

# Sub-diffraction limit nano-photonic waveguides by quantum dot array structure – modeling and simulation

Chia-Jean Wang\*, Lih Y. Lin  
University of Washington, Seattle, WA USA 98195

## ABSTRACT

Building photonic integrated circuits, which overcome the quantum limitation of the uncertainty principle, requires a new paradigm for optical waveguide design that is fundamentally different from the conventional approach. With recent advances in creating nanomaterials, quantum dots made of semiconductor compounds have enabled manipulation of electron and photon interaction in the presence of optical or electrical stimulus. In this paper, we explore the frontier of using quantum dots in new waveguide structures to pave the way for devices whose dimensions are below the diffraction limit of light. These components handle signals in the optical domain, and exploit the high-speed and transparency advantages of light. We first calculate the gain spectrum for pulsed optically-pumped quantum dots and derive the gain coefficient for waveguides. Then, a new model for a quantum dot waveguide is presented and optimum waveguide structure for propagation is determined. The results for two material systems, CdSe and CdTe quantum dots operating in free space, are given throughout. The model may be applied and extended to other compounds and establishes a foundation for quantum dot nano-scale photonic integrated circuits. By utilizing the non-linear properties of quantum dots, the proposed device forms a basis for applications in sensing, computing, and signal processing.

Keywords: Quantum dot, photonic integrated circuit, nano-scale waveguide, sub-diffraction limit, optical gain spectrum.

## 1. INTRODUCTION

In order to fabricate devices that may greatly improve current data transmission rates as well as processing capacity, techniques that do not rely on optical lithography are being explored. However, the basis for high-density circuits, especially those photonic in nature, begins with a waveguiding or energy transfer scheme that can be closely spaced. While conventional methods are limited by Heisenberg's Uncertainty Principle, there are some options that propose sub-diffraction limit propagation. In particular, one possibility uses aligned metal nanoparticles to transmit plasmonic excitation across a distance<sup>1,2</sup>. However, loss, fabrication and the lack of interchangeable optical-electronic-plasmon energy conversion mechanisms provide considerable challenges.

On the other hand, a negative dielectric structure has been suggested to enable waveguiding at the nanometer scale<sup>3</sup>. The concept involves a cladding material of high refractive index surrounding a core of negative dielectric instead of a low value positive dielectric. Nevertheless, incorporation of the waveguide to other on-chip integrated devices would still prove to be a barrier in subsequent system design in addition to the first step of fabricating the structure itself. Similarly, nanoribbons on the order of 100 nm wide by 400 nm thick have been created and show viability for flexible guiding of light in the UV and visible range over hundreds of micrometer in length<sup>4</sup>. Preliminary work indicates that the device may serve as wavelength specific filters and common waveguide structures such as Mach-Zender interferometers and couplers although the losses are large at an estimated 1-8 dB/mm and compatibility with electronic applications remains an issue.

To provide another solution, we propose a quantum dot array nano-photonic waveguide. The QD, originally utilized to generate low threshold current lasers<sup>5,6,7</sup>, is finding many uses in recent technologies. For instance, when conjugated to the protein compatible molecules, QDs may serve as high extinction coefficient optical labels in biological assays<sup>8,9</sup>. An optical switch composed of three quantum dots has been demonstrated as well<sup>10</sup> and the implementation of a quantum dot based optical transistor has been put forth<sup>11</sup>. In addition to developments in the photonic realm<sup>12,13</sup>, all applications

---

\*[jeanwang@ee.washington.edu](mailto:jeanwang@ee.washington.edu); phone 1 206 616 4785; fax 1 206 543 3842

capitalize on the unique properties of the QD. Namely, the semiconductor material can be selected to confine a varying number of electron and hole states. Furthermore, the QD may be further customized to emit the desired photon energy ranging from ultraviolet to infrared by adjusting the device dimension and material composition. The principle relies on generating an electron-hole pair in the quantum dot by providing enough energy to boost electrons in the conduction band to the valence band. For either a core/shell or core QD, the exciton is restricted to the core length with the minimum bandgap energy. In the former case, the shell forms a potential well with the core while for a core only device, an infinite well is assumed. Subsequently, during electron-hole recombination, the photon will have an energy equal to the separation between the states.

As electrons may be excited and used for stimulated emission, quantum dot operation is thus capable of gain, which can be used to lessen loss over an energy transmission length. However, in order to determine the behavior of a waveguide constructed of quantum dots, a model of the device response given optical pumping and signal input conditions is needed. Consequently, we analyze the effects of optically pumped QDs in terms of absorption, emission and gain in part 2, starting with a description of the device in section 2.1. Electrical pumping operation of the QD is discussed in section 2.2 and serves as a contrast to the optical pulsed pumping model in section 2.3. The gain coefficient is found in section 2.4 while the results for quantum dots of two semiconductor systems, CdSe and CdTe, are provided in corresponding manner. Section 3 then describes the optical propagation model for a QD waveguide and provides the relative output intensity calculation for an array of five QDs. Lastly, a brief review is found in section 4.

## 2. OPTICAL GAIN MODEL

### 2.1 Nano-photonic waveguide structure

The proposed nano-photonic QD waveguide is depicted in Fig. 1, where an array of QDs is deposited on a silicon substrate through self-assembly. A pump light enables optical gain by shining from above to uniformly excite the QDs at an energy equivalent to the difference of the second heavy hole state in the valence band to the second electron state in the conduction band. A signal light of energy corresponding to the separation of the ground state electron and heavy hole is applied to the waveguide's edge to cause stimulated emission. At an adequate coupling efficiency between QDs, light will propagate through the waveguide and allow sub-diffraction limit energy transfer.

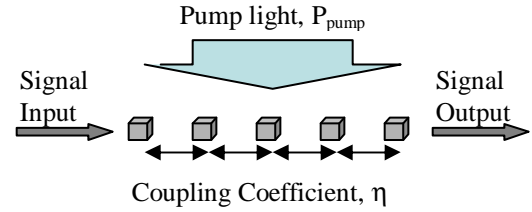


Fig. 1. Schematic drawing of self-assembled QD waveguide.

### 2.2 Electrical pumping

As a successor to quantum well heterostructure lasers, quantum dots have been modeled primarily with electrical pumping. Consequently, gain and threshold current for the device depend on the concentration of dopants or the injection current which dictates the quasi-Fermi level energies,  $E_{fc}$  and  $E_{fv}$ <sup>14,15</sup>. Both  $E_{fc}$  and  $E_{fv}$  may be determined in a straight-forward fashion through the carrier densities,  $n$  and  $p$  ( $\sim n$ ), which are functions of the enveloping Fermi levels,  $f_c$  and  $f_v$ , the QD dimensions and the discrete electron and hole energies,  $E_{clmn}$  and  $E_{hlmn}$ . Accordingly,

$$n = \sum_{lmn} \frac{2}{\left[1 + \exp\left(\frac{E_{clmn} - E_{fc}}{kT}\right)\right] L_x L_y L_z} = \sum_{lmn} \frac{2 \cdot f_c(E_{clmn})}{L_x L_y L_z}, \text{ and} \quad (1)$$

$$p = \sum_{lmn} \frac{2}{\left[1 + \exp\left(\frac{E_{fv} - E_{hlmn}}{kT}\right)\right] L_x L_y L_z} = \sum_{lmn} \frac{2 \cdot (1 - f_v(E_{hlmn}))}{L_x L_y L_z}, \quad (2)$$

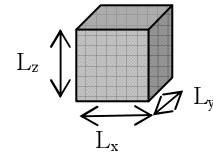


Fig. 2. Diagram of core quantum box.

with  $L_x$ ,  $L_y$  and  $L_z$  being the lengths of the quantum dot when treated as a quantum box, shown in Fig. 2. The electron spin states are accounted for by the factor of two in the numerator and all confined energy states of the quantum dot are considered through the summation over each combination of  $l$ ,  $m$  and  $n$ . For a quantum dot made of two semiconductors each defining the core and shell portions, the conduction band offsets,  $\Delta E_c$  and  $\Delta E_v$ , and material parameters determine the quantized energies. In contrast, a core QD operating in free space is modeled with infinite band offsets such as for an infinite potential well. Table I lists the relevant bandgap energies and effective electron and heavy hole masses for CdSe and CdTe core QDs. Additionally, for core and core/shell cases, the number of electron-hole levels to simulate is adjusted to account for the signal input or electron-hole pair recombination energy.

TABLE I  
Bandgap Energy and Effective Electron/Hole Mass

Core	$E_{g,1,200K}$ (eV)	$m_e/m_{hh}$
CdSe	1.7	0.11/0.44
CdTe	1.56	0.11/0.35

After substitution of the device constants, the quasi-Fermi energies provide the only unknown in (1) and (2) and can be subsequently calculated and used to determine the linear absorption coefficient,  $\alpha(\omega)$ , and linear emission coefficient,  $e(\omega)$ , components in the QD<sup>14</sup>:

$$\alpha(\omega) = \frac{\omega}{n_r} \sqrt{\frac{\mu_0}{\epsilon_0}} \sum_{lmn} \int_{E_g}^{\infty} \langle \mathbf{R}_{ch}^2 \rangle \frac{g_{ch} f_v(E_1) [1 - f_c(E_2)] \hbar / \tau_{in}}{(E_{ch} - \hbar\omega)^2 + (\hbar / \tau_{in})^2} dE_{ch}, \quad (3)$$

$$e(\omega) = \frac{\omega}{n_r} \sqrt{\frac{\mu_0}{\epsilon_0}} \sum_{lmn} \int_{E_g}^{\infty} \langle \mathbf{R}_{ch}^2 \rangle \frac{g_{ch} f_c(E_2) [1 - f_v(E_1)] \hbar / \tau_{in}}{(E_{ch} - \hbar\omega)^2 + (\hbar / \tau_{in})^2} dE_{ch}. \quad (4)$$

The refractive index is  $n_r$  while  $\mathbf{R}_{ch}$  represents the dipole moment, which may be expressed as:

$$\langle \mathbf{R}_{ch}^2 \rangle = R^2 (k_y^2 + k_z^2) / k^2 \cdot \delta_{ll'} \delta_{mm'} \delta_{nn'}, \text{ with } R^2 = \left( \frac{e\hbar}{2E_{ch}} \right)^2 \frac{E_g (E_g + \Delta_0)}{(E_g + 2\Delta_0 / 3)m_c} \quad (5)$$

where  $\Delta_0$  is the spin-orbit splitting value,  $m_c$  is the conduction band effective mass and  $k_y$ ,  $k_z$  are the wave vector components of  $\mathbf{k}$ . The density of states for a quantum dot is  $g_{ch}$ , or explicitly:

$$g_{ch} = 2 \delta(E_{ch} - E_{clmn} - E_{hlmn} - E_g) / (L_x L_y L_z). \quad (6)$$

The intraband relaxation time,  $\tau_{in}$ , is 1 ps for CdSe<sup>16</sup> and 0.5 ps CdTe<sup>17</sup>. Furthermore, the Fermi functions are evaluated at  $E_1$  and  $E_2$ , which are defined as the electron energy levels in the valence and conduction band, respectively. Both (3) and (4) are stated as rates of absorption and emission per unit length of the QD such that the overall device gain is:

$$G(\omega) = e(\omega) - \alpha(\omega), \text{ or } G(\omega) = \frac{\omega}{n_r} \sqrt{\frac{\mu_0}{\epsilon_0}} \sum_{lmn} \int_{E_g}^{\infty} \langle \mathbf{R}_{ch}^2 \rangle \frac{g_{ch} [f_c(E_2) - f_v(E_1)] \hbar / \tau_{in}}{(E_{ch} - \hbar\omega)^2 + (\hbar / \tau_{in})^2} dE_{ch}. \quad (7)$$

While the formulae in (1) through (7) are valid under electrical pumping condition, they are also relevant to the optical pumping case. The differences in analysis are discussed in the ensuing section.

### 2.3 Pulsed optical pumping

In an optically pumped system, the carrier concentrations within the quantum dot,  $n$  and  $p$ , are not constant with injection current or specified by doping levels. Instead, the number of free carriers fluctuates depending on the material absorption rate and pump power. Referring back to Fig. 1, a laser source is placed above the waveguide such that all the QDs may absorb photons and excite electrons in the valence band into the conduction band simultaneously. Then, an optical signal shines incident to the waveguide edge to prompt electrons to fall back to their original states and stimulate emission of photons, which couple to adjacent QDs in the near-field to induce wave propagation. However, with each electron-hole pair generation or recombination, the energy required to excite electrons to a vacant state increases or decreases causing the rates of absorption and emission and hence, the quasi-Fermi

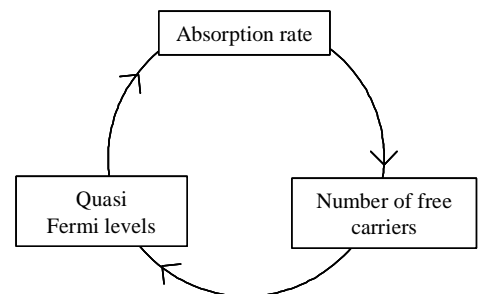


Fig. 3. Inter-dependence of various parameters in an optically-pumped quantum dot.

levels to change. Consequently, the system reflects back upon itself in a manner depicted in Fig. 3, where  $n$  and  $p$  variations affect the quasi-Fermi levels used to determine absorption and hence, the number of free carriers that the system may support. As a result, the gain solution will be unique given each set of pump conditions.

For a pulsed source, the criteria for stimulated emission is that the pulse duration be less than the time for electron-hole recombination,  $\Delta t < \tau_r$ , while at the same time, long enough to enable population inversion among the electrons. With the restriction in place, we can presume that all free carriers available after considering spontaneous emission rates will recombine due to the signal input. Together with  $\Delta t$ , the other pump light variables such as frequency,  $\omega_p$ , and magnitude in power,  $P_{\text{pump}}$ , help define the number of free carriers in a QD. Given that the source is incident on the x-y plane of the quantum box with z being the measure of depth, we have:

$$n \cong p = \frac{P_{\text{pump}}}{L_x L_y \cdot \hbar \omega_p} \Delta t \alpha(\omega_p) \quad (8)$$

with  $\alpha(\omega_p)$  as the absorption rate by the quantum dot at the particular pulse frequency. Another constraint of the system is that there exists a minimum pump energy at  $E_g + E_{h000} + E_{c000}$ , which defines the lowest state transition between the valence and conduction bands. In our simulations, the pump energy is set at the amount required to excite an electron occupying the first state in the valence band to the first state in the conduction band. Likewise, the signal light is designed to have an energy equal to the ground state separation of the valence and conduction bands. In this manner, the pump light and signal input are distinct and avoid mixing in the waveguide.

Combining (8) with (1) and (2), the revised carrier densities may be found and further reduced to a form giving the number of free carriers within the quantum dot:

$$N = \frac{P_{\text{pump}}}{\hbar \omega_p} \Delta t \alpha(\omega_p) L_z = \sum_{lmn} \left[ \frac{2}{1 + \exp\left(\frac{E_{clmn} - E_{fc}}{kT}\right)} \right], \quad P = \frac{P_{\text{pump}}}{\hbar \omega_p} \Delta t \alpha(\omega_p) L_z = \sum_{lmn} \left[ \frac{2}{1 + \exp\left(\frac{E_{fv} - E_{hlmn}}{kT}\right)} \right] \quad (9)$$

From (9), we see that N and P are proportional to the rate of photon absorption as well as the pulse time and device depth. As before, known parameters are applied to the equations to determine the quasi-Fermi level energies. The solutions for  $E_{fc}$  and  $E_{fv}$  are then used to calculate absorption, emission and gain from (3), (4), and (7). Since the number of free carriers is tied to the characteristics of the pump light, differences in  $\omega_p$ ,  $P_{\text{pump}}$ , or  $\Delta t$  require a new complete gain solution. The absorption, emission and gain spectra at pump powers from 0.01 nW to 10 nW and 1000 nW to 1 nW are shown in Fig. 4 and 5 for CdSe and CdTe core quantum dots with dimensions of 5 nm  $\times$  5 nm  $\times$  5 nm each. In the simulation,  $E_{\text{pump}} = \hbar \omega_p$  as designed is 3.74 eV for CdSe and 3.71 eV for CdTe with  $\Delta t$  set to 20 ns and 100 ps, respectively. Highest gain is found at wavelengths matching the ground state transition from the conduction to valence band, which are 560.9 nm for the former and 590.6 nm for the latter material. Moreover, full width at half maximum of the gain curves is around 0.5 nm for the selenium and 1 nm for the tellurium compound, which is principally derived from the factor of 2 discrepancy in the intraband relaxation times.

Comparing the curves in further detail, we see that the gain peak is narrower and makes the transition from an absorption to an emission dominant region at a higher pump power for CdSe. However, the trend shows earlier gain saturation for CdTe. The characteristics of the spectra are determined by two main factors. Primarily, the shape of gain at its crest is defined by the intraband relaxation time coupled with the Lorentzian lineshape function approximating homogeneous broadening within each discrete energy state. Secondly, the quasi-Fermi levels, which are solved dynamically for each pump power, set the overall values for gain and locate them at wavelengths matching allowable energy separations.

Since the particles are placed in free space, the number of possible electron and hole states is infinite. However, the energy states under consideration are capped at the first excited levels as confined by the pump energy. As a result, the larger bandgap for CdSe shifts the quasi-Fermi levels away from each other and enhance the separation between absorption and emission to obtain a higher gain. On the other hand, smaller  $E_g$  in CdTe allows lower pump energies to generate electron-hole pairs and enable gain. Thus, the bandgap and input energy provide the underpinnings to quasi-Fermi level effects.

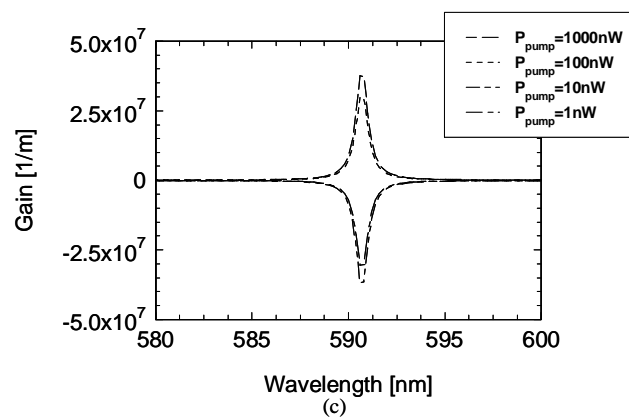
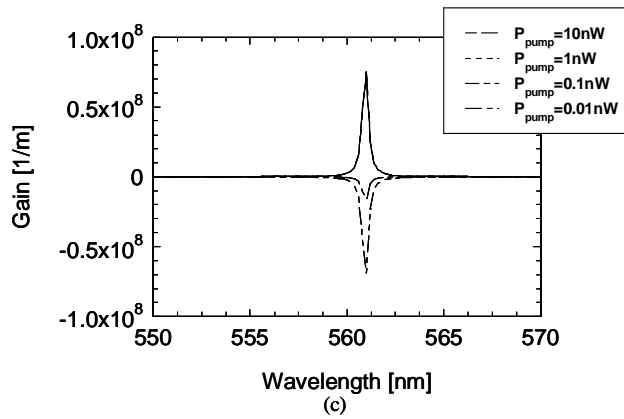
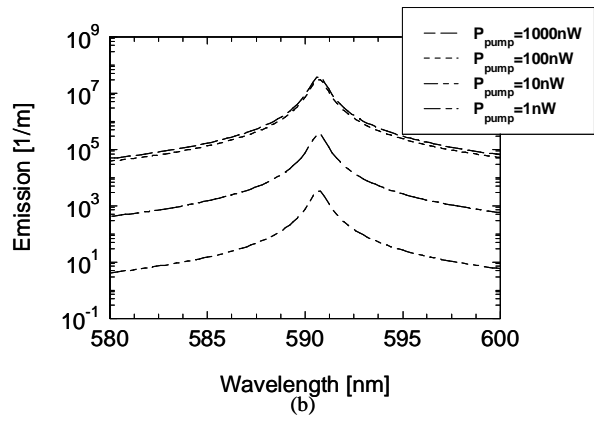
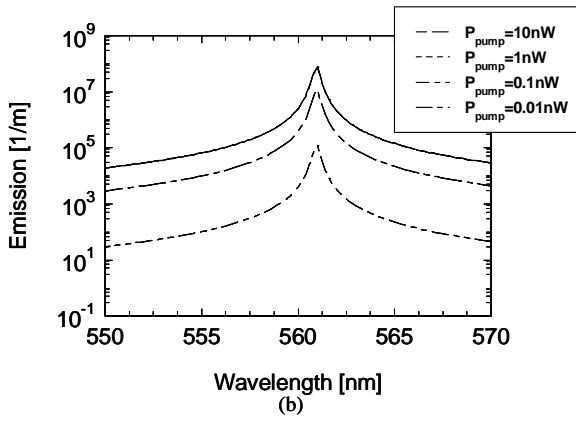
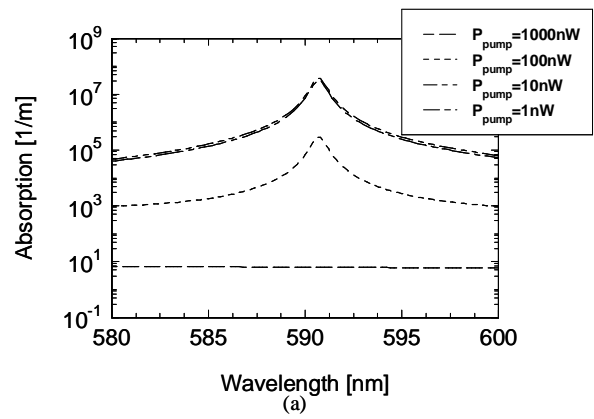
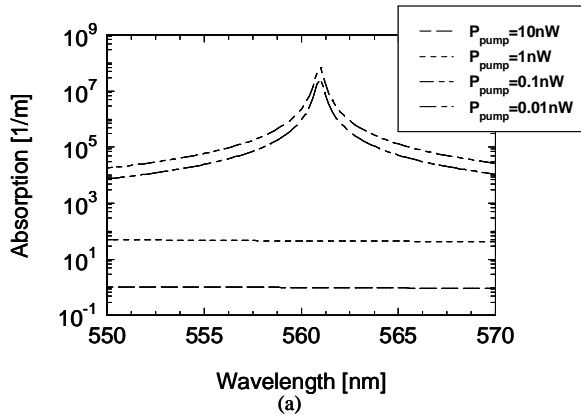


Fig. 4. (a) Absorption, (b) Emission, and (c) Gain Spectra of a  $5\text{ nm} \times 5\text{ nm} \times 5\text{ nm}$  CdSe quantum cube in pulsed operation.

Fig. 5. (a) Absorption, (b) Emission, and (c) Gain Spectra of a  $5\text{ nm} \times 5\text{ nm} \times 5\text{ nm}$  CdTe quantum cube in pulsed operation.

## 2.4 Gain coefficient

To determine the optimal operation range in amplifier systems as well as to compare performance between them, one parameter that is commonly used is the gain coefficient<sup>18</sup>, which is calculated as:

$$\text{gain coefficient} = G(\omega) / P_{\text{pump}} \quad (10)$$

In general, the peak value corresponds to maximum gain over minimum pump power. For the two quantum dot materials under investigation, Fig. 6 and 7 depict the results from (10) with pulsed optical pumping. As the structure dimensions are the same and the bandgap energies are similar, the curves for CdSe and CdTe are closely aligned in shape. Specifically, the gain coefficient changes from negative to positive around 0.13 nW for the former and 60 nW for the latter. Furthermore, the pump power necessary for best device response is at 0.24 nW with CdSe and at 110 nW with CdTe, which has larger overall gain coefficients.

The disparities between the results are mostly caused by the lower pulse duration for CdTe, which increases the pump power necessary to generate electron-hole pairs as well as to induce stimulated emission. On the contrary, higher  $E_g$  for CdSe requires a higher pump energy to enable gain but its effects are overshadowed by those attributed to  $\Delta t$ . The consequences of pump and material differences show up first in the Fermi energies, depicted in Fig. 8 and Fig. 9. The solid vertical lines in the charts specify the amount of quasi-Fermi energy separation for optimal gain coefficient. It is useful to note that the value is measured to be 0.51 eV for CdSe and 0.96 eV for CdTe.

As a side note, changes to the quantum dot dimensions will alter the position of the energy states in the potential well. In particular, increasing the absorption length brings both the discrete allowable energies and resulting Fermi levels closer to each other. A reversed outcome occurs when the size is decreased. Therefore, gain coefficient will be maximized at relatively lower pump powers for larger QDs and higher pump powers for smaller QDs.

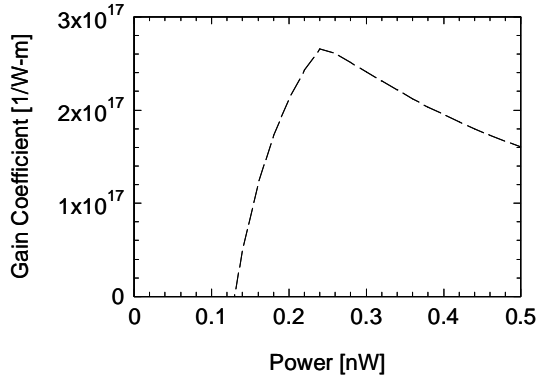


Fig. 6. Pulse gain coefficients near optimal pump power for a 5 nm x 5 nm x 5 nm CdSe QD.

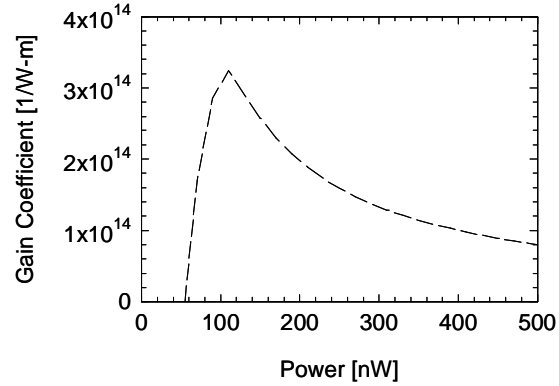


Fig. 7. Pulse gain coefficients near optimal pump power for a 5 nm x 5 nm x 5 nm CdTe QD.

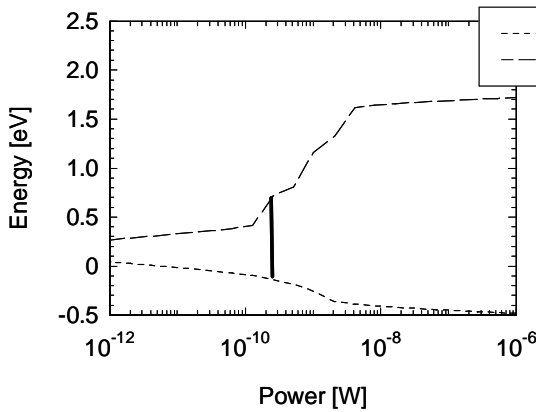


Fig. 8. Fermi levels under pulse-pumping for a 5 nm x 5 nm x 5 nm CdSe QD.

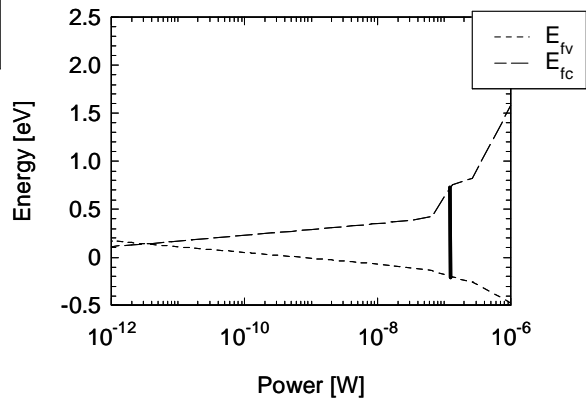


Fig. 9. Fermi levels under pulse-pumping for a 5 nm x 5 nm x 5 nm CdTe QD.

### 3. OPTICAL PROPAGATION MODEL

Besides determining the optical gain behavior of quantum dots, considering the conditions for the energy transfer in an array of QDs is of equal importance. As the device requires a pump light to enable gain by generating electron-hole pairs and a signal input to produce stimulated emission of photons, the two sources together cause optical propagation in the waveguide structure. While the former compensates for loss events and shapes the gain spectra, the characteristics of the latter specify at which point on the curve the device operates. In particular, gain is maximized by selecting a signal light frequency equal to the energy necessary to recombine an electron in the ground state of the conduction band with a hole in the ground state of the valence band.

From the diagram in Fig. 1, we show a case where five quantum dots comprise a waveguide. With the pump light operating and the signal input placed incident to the device edge, photon emission occurs in the first QD. Given a symmetric QD, propagating waves emanate in the forward and backward directions such that photons travel to both ends of the waveguide. In addition, energy transfer between the QDs is modeled with a coupling coefficient for near-field interaction<sup>19</sup>. Consequently, the amount of coupling and the signal amplification represented by the gain value are the two critical parameters for describing the propagation of energy in the structure.

The output intensity for an array of  $N$  quantum dots may be related to the input intensity through multiplication with ABCD matrices. Specifically, the quantum dot matrix ( $M_{QD}$ ) containing the gain term from the material, and a propagation matrix ( $M_{prop}$ ) with the coupling coefficient,  $\eta$ :

$$M_{QD} = \begin{bmatrix} 0 & 1 \\ -1 & 2e^{-G} \end{bmatrix}, \text{ and } M_{prop} = \begin{bmatrix} \eta & 0 \\ 0 & \eta^{-1} \end{bmatrix} \quad (11)$$

provide the main components to express the output intensity existing for two directions, which are “+” for forward propagation away from the signal, and “-” for backwards toward the source:

$$\begin{bmatrix} I_{out,+} \\ I_{out,-} \end{bmatrix} = M_{QD} \cdot (M_{prop} \cdot M_{QD})^{N-1} \cdot \begin{bmatrix} I_{in,+} \\ I_{in,-} \end{bmatrix}. \quad (12)$$

Since no light originates at the opposing edge of the waveguide and moves toward the input edge,  $I_{out,-} = 0$  serves as a simplifying boundary condition. Furthermore, letting the matrix multiplication term be expanded into a final form:

$$M_{total} = M_{QD} \cdot (M_{prop} \cdot M_{QD})^{N-1} = \begin{bmatrix} m_{11} & m_{12} \\ m_{21} & m_{22} \end{bmatrix}, \quad (13)$$

we find that the relative output,  $I_{out}/I_{in}$  becomes:

$$\frac{I_{out,+}}{I_{in,+}} = \frac{I_{out}}{I_{in}} = m_{11} - \frac{m_{12}m_{21}}{m_{22}}. \quad (14)$$

The model is implemented with a range of coupling coefficients for a five QD waveguide to show relative output intensity as a function of unit-less gain in Fig. 10. The values for  $\eta$  vary from 0.1 to 0.9 although an experimental optical switch system involving three quantum dots demonstrated coupling as high as 0.95<sup>19</sup>. We have limited  $I_{out}/I_{in}$  to a maximum of 1 in the chart for a practical reason. Like other amplification structures such as lasers and erbium doped fiber amplifiers, the device output cannot keep increasing with fixed and finite pump or signal power. Since there is a restricted number of electrons that may be excited due to the escalating energy required to continue generating electron-hole pairs, there is also a corresponding saturation point in the output intensity<sup>18</sup>. On the whole, the QD materials and the pump and signal frequencies determine the optimum performance of the waveguide.

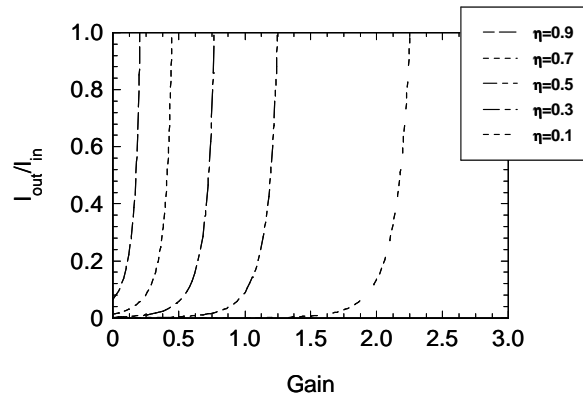


Fig. 10. Output versus input intensity as a function of gain through each quantum dot given a range of coupling coefficients between adjacent quantum dots for a 5 QD waveguide.

The trend in Fig. 10 shows that gain and coupling may compensate for each other in attaining a specific output. Moreover, the curves for larger coupling coefficients depict a steeper rise for  $I_{\text{out}}/I_{\text{in}}$ , which confirms that near-field coupling plays a crucial role in energy transfer between QDs designed to operate at a set gain. Using the  $5 \text{ nm} \times 5 \text{ nm} \times 5 \text{ nm}$  CdSe quantum dot as an example, we cross-reference with Fig. 4c to find a maximum gain of  $7.47 \times 10^7 \text{ 1/m}$  which yields 0.375 when multiplied with the QD absorption length dimension. Assuming  $\eta$  is between 0.7 and 0.9, the resulting  $I_{\text{out}}/I_{\text{in}}$  will fall within the range of 0.2 to 1, respectively. Indeed, sub-diffraction limit propagation will be severely restricted by reduced  $\eta$  resulting from quantum dots which are spaced more than tens of nanometers apart<sup>19</sup>. The last point is critical for inhibiting crosstalk between neighboring quantum dot array waveguides.

#### 4. CONCLUSION

We proposed that a nano-photonic waveguide fabricated of quantum dots may enable sub-diffraction limit energy propagation. A model was developed to calculate absorption, emission and gain of the QD under optically pulsed pump conditions as well estimate the optical transfer behavior for a 1D array waveguide. The results indicate that the intensity at the ending edge of the waveguide may be maintained through an effective combination of device gain and coupling efficiency, whereby a high gain value would compensate for lower inter-dot coupling and vice versa. With an increasing number of QDs, sustained propagation would require an overall higher gain and coupling efficiency. While two systems, CdSe and CdTe, were investigated, the model may be applied to QDs of other semiconductor materials and serves as a basis for applications of wider reach. Indeed, given its gain mechanism, nanometer dimensions and ability to act as an interface between electrons and photons, the quantum dot is an attractive candidate for providing the foundation of high density photonic circuits.

#### REFERENCES

1. M. L. Brongersma, J. W. Hartman, and H. A. Atwater, "Electromagnetic energy transfer and switching in nanoparticle chain arrays below the diffraction limit," *Phys. Rev. B*, **62:24**, R16356-R16359, 2000.
2. S. A. Maier, P. G. Kik, H. A. Atwater, S. Meltzer, E. Harel, B. E. Koel, and A. A. G. Requicha, "Local detection of electromagnetic energy transport below the diffraction limit in metal nanoparticle plasmon waveguides," *Nature Materials*, **2:4**, 229-32, 2003.
3. J. Takahara, S. Yamagishi, H. Taki, A. Morimoto, and T. Kobayashi, "Guiding of a one-dimensional optical beam with nanometer diameter," *Optics Lett.*, **22:7**, 475-478, 1997.
4. M. Law, D. J. Sirbuly, J. C. Johnson, J. Goldberger, R. J. Saykally, and P. Yang, "Nanoribbon waveguides for subwavelength photonics integration," *Science*, **305**, 1269-1273, 2004.
5. R. Dingle and C. H. Henry, "Quantum effects in heterostructure lasers," U.S. Patent 3,982,207, Sept. 21, 1976.
6. N. N. Ledentsov, M. Grundmann, F. Heinrichsdorff, D. Bimberg, V. M. Ustinov, A. E. Zhukov, M. V. Maximov, Z. I. Alferov, and J. A. Lott, "Quantum-dot heterostructure lasers," *IEEE J. Select. Topics Quantum Electron.*, **6:3**, 439-451, 2000.
7. V. M. Ustinov, A. E. Zhukov, A. Y. Egorov, and N. A. Maleev, *Quantum Dot Lasers*, Oxford University Press, Oxford, 2003.
8. W. C. W. Chan and S. Nie, "Quantum dot bioconjugates for ultrasensitive nonisotopic detection," *Science*, **281**, 2016-2018, 1998.
9. M. Bruchez Jr., M. Moronne, P. Gin, S. Weiss, and A. P. Alivisatos, "Semiconductor nanocrystals as fluorescent biological labels," *Science*, **281**, 2013-2016, 1998.
10. M. Ohtsu, K. Kobayashi, T. Kawazoe, and T. Yatsui, "Nanophotonics: design, fabrication, and operation of nanometric devices using optical near fields," *IEEE J. Select. Topics Quantum Electron.*, **8:4**, 839-862, 2002.
11. M. LoCascio, C. T. Ballinger, D. P. Landry, and J. E. Reynolds, "Optical switch having a saturable absorber," U.S. Patent 6 571 028, May 27, 2003.
12. H. Cao, J. Y. Xu, W. H. Xiang, Y. Ma, S.-H. Chang, S. T. Ho, and G. S. Solomon, "Optically pumped InAs quantum dot microdisk lasers," *Applied Physics Letters*, **76:24**, 3519-3521, 2000.
13. O. Benson and Y. Yamamoto, "Master-equation model of a single-quantum-dot microsphere laser," *Phys. Rev. A*, **59:6**, 4756-4763, 1999.
14. M. Asada, Y. Miyamoto, and Y. Suematsu, "Gain and the threshold of three-dimensional quantum-box lasers," *IEEE J. Quantum Electron.*, **22:9**, 1915-1921, 1986.

15. K. J. Vahala, "Quantum box fabrication tolerance and size limits in semiconductors and their effect on optical gain," *IEEE J. Quantum Electron.*, **24:3**, 523-520, 1988.
16. P. Guyot-Sionnest, M. Shim, C. Matranga, and M. Hines, "Intraband relaxation in CdSe quantum dots," *Phys. Rev. B*, **60:4**, R2181-R2184, 1999.
17. R. E. Marotti, S. Tsuda, and C. H. de Brito Cruz, "Intraband Ultrafast Relaxation in CdTe Quantum Dots Dispersed in a Glass Matrix," *Brazilian J. of Physics*, **26:1**, 193-197, 1996.
18. C. R. Giles, and E. Desurvire, "Modeling erbium-doped fiber amplifiers," *J. Light. Technol.*, **9:2**, 271-283, 1991.
19. T. Kawazoe, K. Kobayashi, S. Sangu, and M. Ohtsu, "Demonstrating nanophotonic switching using near-field pump-probe photoluminescence spectroscopy of CuCl quantum cubes," *J. Microsc.*, **209**, 261-266, 2003.